Texture Mediated Grain Boundary Network Design in Three Dimensions

Oliver K. Johnson[a,b,*], Christopher A. Schuh[b]

[a]*Department of Mechanical Engineering, Brigham Young University, Provo, UT 84602*
[b]*Department of Materials Science and Engineering, Massachusetts Institute of Technology, Cambridge, MA 02139, USA*

Abstract

Experimental grain boundary engineering studies have demonstrated the potential for materials properties enhancement via the modification of grain boundary network structure. These techniques apply to materials that readily form annealing twins and are amenable to cyclic thermomechanical processing and have resulted in dramatic property enhancement. In this work we present a theoretical framework that enables the design of grain boundary networks in polycrystalline materials through an alternative approach: exploitation of a relationship between crystallographic texture and grain boundary network structure. Because crystallographic texture is a universal characteristic of polycrystalline materials, this work has the potential to significantly expand the class of materials whose grain boundary networks can be controlled. We demonstrate the utility of the approach by application to a concrete design problem involving competing design objectives for yield strength, elastic compliance, and resistance to electromigration. We construct the first materials properties closure to comprise grain boundary network sensitive properties and identify an optimal microstructure that is predicted to outperform an undesigned isotropic material.

Keywords: Grain Boundary Engineering, Grain Boundary Network, Crystallographic Texture, Microstructure Design, Triple Junction

1. Introduction

Numerous experimental studies have demonstrated the possibility of improving the performance of materials by manipulating the structure of the grain boundary network [1–5]. The modern practice of grain boundary engineering (GBE) consists of cyclic thermomechanical processing aimed at increasing the population of coherent twins in a material and has resulted in orders of magnitude improvements in properties. However, because these techniques exploit the ability of certain materials to form annealing twins, traditional GBE is limited in its application to those materials that exhibit this behavior.

The present work attempts to build on prior GBE research by developing a theoretical framework that facilitates the design and optimization of GB networks (GBNs). By taking a texture-mediated approach—i.e. by leveraging a recently established connection between crystallographic texture and GBN structure [6, 7]—we present methods applicable to arbitrary crystalline materials including those that do not readily form annealing twins or are not amenable to cyclic thermomechanical processing. The framework developed here allows one to design the GBN structure of a polycrystal, not just to improve its performance with respect to a single property; rather, it facilitates the optimization of microstructure for complex *multi*-objective design problems. Our approach builds upon the general spectral methodology that has been used in the past for texture sensitive properties [8], expanding it to comprise grain boundary networks and their properties.

For the sake of clarity and to illustrate its utility, we will develop the theory in the context of a hypothetical design problem. First, we will define the design problem and specify the design constraints and objectives. We will then develop relevant structure-property models. Using these models and microstructure hulls like those described in [6], we will construct the envelope of all possible combinations of the properties relevant to the design problem and identify the microstructure that

---

*Corresponding Author: Tel. +1-801-422-0972
Email addresses: ojohnson@byu.edu (Oliver K. Johnson), schuh@mit.edu (Christopher A. Schuh)

optimally satisfies the design objectives.

2. Design Problem

As a purely hypothetical illustrative example, consider microstructure sensitive design [8, 9] of aluminum interconnects for flexible electronics. Chemistry and geometry will be held constant and we will seek to optimize the microstructure of a polycrystalline Al sample in order to satisfy the following design constraints and objectives relevant to the chosen application:

$$\mathbf{max}\ \overline{\sigma_{y1}} \tag{1a}$$

$$\overline{S_{1111}} = S_{1111}^{sub} \tag{1b}$$

$$\mathbf{min}\ \overline{D} \tag{1c}$$

In Eq. 1, the overline denotes an effective property of the polycrystalline aggregate. $\overline{\sigma_{y1}}$ represents the effective yield strength of the polycrystalline sample when tension is applied along the sample x-direction. Maximizing $\overline{\sigma_{y1}}$ will reduce the risk of plastic deformation under static load and improve the fatigue properties of the interconnect material [10]. Minimizing the effective diffusivity of the grain boundary network, $\overline{D}$, will improve resistance to electromigration as the mean time to failure (MTF) via electromigration is inversely proportional to $\overline{D}$ (see [11] and Section 7 of the present work). $\overline{S_{1111}}$ is the elastic compliance of the polycrystal in the sample x-direction, which we require to match that of the substrate, S_{1111}^{sub}, to which it is applied.

Microstructure sensitive models for $\overline{S_{1111}}$ and $\overline{\sigma_{y1}}$ are readily available. Below, we explain the application of each of these structure-property models to the present design problem. We also develop a model for $\overline{D}$ that depends on the types and populations of grain boundaries and triple junctions present in the polycrystal.

3. Conventions

3.1. Orientations and Misorientations

In this work, a crystal orientation, $q = [a, b, c, d]$, is represented by a unit quaternion, whose elements are related to the corresponding rotation angle, ω, and spherical angles of the rotation axis, (θ, ϕ), by [12, 13]:

$$\begin{aligned}
a &= \cos(\omega/2) \\
b &= \sin(\omega/2) \sin\theta \cos\phi \\
c &= \sin(\omega/2) \sin\theta \sin\phi \\
d &= \sin(\omega/2) \cos\theta
\end{aligned} \tag{2}$$

with $\theta \in [0, \pi]$ describing the polar angle measured from the positive z-axis, $\phi \in [0, 2\pi)$ the azimuthal angle measured from the positive x-axis, and $\omega \in [0, 2\pi)$.

The orientation of the i-th grain in a polycrystal is denoted by q_i. The lattice misorientation between grains i and j is defined by:

$$q_{ij} = q_i^{-1} q_j \tag{3}$$

where the inverse operation for unit quaternions is defined by [14]

$$q^{-1} = [a, -b, -c, -d] \tag{4}$$

3.2. Statistical Descriptions of the Microstructure

An orientation distribution function (ODF) is denoted by $f(q)$, where the quantity $f(q)\,dq$ provides the probability of observing a grain with orientation infinitesimally close to q. Central to the design methodology of this paper is the expression of distribution functions and constitutive models in spectral form. An ODF can be expanded as a linear combination of hyperspherical harmonics according to [6, 7, 15]:

$$f(q) = \sum_{n=0,2,\ldots}^{\infty} \sum_{l=0}^{n} \sum_{m=-l}^{l} c_{l,m}^n Z_{l,m}^n(q) \tag{5}$$

Our conventions regarding normalization, definitions of the basis functions, computation of the coefficients, and the invariant measure for integration are provided in [7]. Because the hyperspherical harmonic basis functions employed in this expansion may be viewed as a generalization of the well known Fourier series, we refer to this as the Fourier basis. We refer to the expression of functions in this manner as their Fourier representation.

A second equivalent spectral representation of an ODF may be given in the basis of generalized Dirac delta functions and we refer to this as the Dirac representation:

$$f(q) \approx \sum_{j=1}^{J} p_j' \delta(q, {}^j q) \tag{6}$$

where the approximation becomes exact as $J \to \infty$. In this expression, the coefficients p_j' encode the probability of observing an orientation ${}^j q$, belonging to the set of *fundamental orientations*, $\left\{ {}^1q, {}^2q, \ldots, {}^Jq \right\}$, which itself constitutes a discretization of the relevant orientation fundamental zone.

The statistical description of GBNs is complicated by the fact that GB misorientations are not independent (and cannot therefore be assigned randomly from a known distribution). For example, at a triple junction there are three grain orientations which can be assigned from an ODF and are all three independent of one another, but the three resulting GB misorientations coordinating the triple junction are not independent of one another since they derive from the grain orientations. In fact only two misorientations are independent at the triple junction, with the third being fully specified by the constraint of crystallographic consistency [6, 7, 16, 17].

A statistical description of the GBN that satisfies these crystallographic constraints is given by the triple junction distribution function (TJDF) [6, 7], which we denote by $T(q_{12}, q_{23})$. In this statistical treatment, a triple junction is characterized by the ordered pair of its independent grain boundary misorientations (q_{12}, q_{23}). The TJDF admits a spectral representation in the basis of bipolar hyperspherical harmonics according to [6, 7]:

$$T(q_{12}, q_{23}) = \sum_{\substack{n_1, \lambda_{12}, \mu_{12} \\ n_3, \lambda_{23}, \mu_{23}}} t^{n_3, \lambda_{23}, \mu_{23}}_{n_1, \lambda_{12}, \mu_{12}} Z^{n_1}_{\lambda_{12}, \mu_{12}}(q_{12}) Z^{n_3}_{\lambda_{23}, \mu_{23}}(q_{23})$$

(7)

The Dirac basis representation of the TJDF is given by [6]:

$$T(q_{12}, q_{23}) \approx \sum_{k=1}^{K} p_k \delta\left[\left(q_{12}, q_{23}\right), \left({}^k q_{12}, {}^k q_{23}\right)\right] \quad (8)$$

where p_k provides the probability of observing a triple junction associated with the k-th *fundamental triple junction*: $\left({}^k q_{12}, {}^k q_{23}\right)$.

4. Microstructure Hulls

With the microstructures defined statistically by the distribution functions $f(q)$ and $T(q_{12}, q_{23})$, each expressed in spectral form, it is possible to define the corresponding *microstructure hulls*, which encompass all physically realizable ODFs and TJDFs, respectively, and constitute our design spaces. The set of coefficients for a given distribution function can be thought of as coordinates, so that different distributions having distinct values of their coefficients are represented by distinct points in the corresponding space. Thus, the coefficient coordinates of a given distribution function can be written as a vector, which we denote in bold font, e.g.

$\boldsymbol{c} = \left\{c^0_{0,0}, c^2_{0,0}, c^2_{1,-1}, \ldots\right\}$. The *microstructure set*, is defined as the set of coefficient vectors for Dirac delta distributions centered at each of the fundamental orientations or triple junctions, respectively. We refer to the microstructure set for crystallographic textures as the *texture set* and denote its Fourier basis representation by

$$m^{(1)}_S = \left\{ {}^j\boldsymbol{c} \mid {}^j\boldsymbol{c} = \left({}^j c^0_{0,0}, {}^j c^2_{0,0}, {}^j c^2_{1,-1}, \ldots\right),\right.$$
$$\left. {}^j c^n_{l,m} = Z^{n*}_{l,m}\left({}^j q\right), {}^j q \in \mathscr{A}^{(1)}, j \in [1, J] \right\} \quad (9)$$

where $\mathscr{A}^{(1)}$ is the *asymmetric region* or *fundamental zone* for the relevant crystal symmetry point-group. The Dirac basis representation of the texture set is denoted

$$M^{(1)}_S = \left\{ {}^j\boldsymbol{p}' \mid {}^j\boldsymbol{p}' = \left({}^j p'_1, {}^j p'_2, \ldots, {}^j p'_J\right),\right.$$
$$\left. {}^j p'_r = \delta_{rj}, j \in [1, J] \right\} \quad (10)$$

We refer to the microstructure set for TJDFs as the *triple junction set* and denote its Fourier and Dirac basis representations by $m^{(3)}_S$ and $M^{(3)}_S$, respectively. Explicit mathematical definitions for $m^{(3)}_S$ and $M^{(3)}_S$ are provided in [6], and are omitted here for brevity.

Our notation follows that of [6] and it will be observed that this convention uses the parenthetical superscript to denote the order of the microstructure set. Texture is a 1-point statistical description of the microstructure, and thus the notation bears a superscript of [1], while the TJDF is effectively a type of 3-point statistical description of the microstructure and is therefore denoted by a superscript of [3]. As is evident from Eqs. 9–10 we denote the Fourier basis by a lower-case m and the Dirac basis by an upper-case M. When referring abstractly to a microstructure set or hull without regard for a particular basis, we use a script font $\mathscr{M}$.

The microstructure hull is the convex hull of the microstructure set and strictly bounds the space of all possible distributions of the respective microstructural feature [8]. Following our previous nomenclature, we refer to the microstructure hull for crystallographic texture as the *texture hull* and denote its Fourier basis representation by

$$m^{(1)}_H = \left\{ \boldsymbol{c} \mid \boldsymbol{c} \approx \sum_{j=1}^{J} p'_j {}^j\boldsymbol{c}, {}^j\boldsymbol{c} \in m^{(1)}_S, \right.$$
$$\left. 0 \le p'_j, \sum_{j=1}^{J} p'_j = 1 \right\} \quad (11)$$

The Dirac basis representation of the texture hull is denoted

$$M_H^{(1)} = \left\{ \boldsymbol{p'} \ \middle| \ \boldsymbol{p'} = (p_1', p_2', \ldots, p_J'), \right.$$

$$\left. 0 \le p_j', \ \sum_{j=1}^{J} p_j' = 1 \right\} \quad (12)$$

Finally, we refer to the microstructure hull for TJDFs as the *triple junction hull* and denote its Fourier and Dirac basis representations by $m_H^{(3)}$ and $M_H^{(3)}$, respectively. Again, explicit mathematical definitions for $m_S^{(3)}$ and $M_S^{(3)}$ are provided in [6].

The microstructure hull is a closed convex region that constitutes the design space for microstructure design problems. For the present problem we will employ the texture hull and a subspace of the triple junction hull that contains microstructures for which spatial correlations in grain orientation are absent. The Fourier basis representation of this *uncorrelated triple junction hull* was defined in [6] and is denoted $\widetilde{m}_H^{(3)}$. We will define the Dirac basis representation, denoted $\widetilde{M}_H^{(3)}$, in Section 6.4.

5. Constitutive Models

Our objective is to develop the mathematical apparatus whereby the structure of grain boundary networks can be optimized for a given engineering application. Our method employs spectral representations of microstructural statistics, as already described, in concert with spectral representations of the relevant constitutive models. For elasticity and initial plastic yield we employ constitutive models that are sensitive to crystallographic texture. For diffusivity we develop a constitutive model that is sensitive to the structure of the grain boundary network.

5.1. Yield

The effective macroscopic yield strength of our polycrystalline material can be approximated using the model developed by Sachs [18, 19], according to:

$$\overline{\sigma_{y1}} \approx \tau_{CRSS} \left(\overline{ \frac{1}{\max\limits_{\alpha} \left| b_1^\alpha(q)\, n_1^\alpha(q) \right| } } \right) \quad (13)$$

where τ_{CRSS} is the critical resolved shear stress (0.79 MPa for Al [20]), and $b_1^\alpha(q)$ and $n_1^\alpha(q)$ are the x-components of the slip direction and slip plane

normal, respectively, of the α-th slip system—both of which are functions of the crystallographic orientation, q, in a given grain. The overbar in Eq. 13 indicates a volume average over all crystal orientations in the polycrystal, which can be expressed explicitly as

$$\overline{\sigma_{y1}} \approx \tau_{CRSS} \int_{S^3} f(q) \left(\frac{1}{\max\limits_{\alpha} \left| b_1^\alpha(q)\, n_1^\alpha(q) \right|} \right) \mathrm{d}q \quad (14)$$

where $f(q)$ is an ODF and the integration is performed with respect to the appropriate invariant measure: $\mathrm{d}q = \frac{1}{2} \sin^2(\omega/2) \sin\theta \mathrm{d}\omega \mathrm{d}\theta \mathrm{d}\phi$.

Substituting the Fourier representation of an ODF (Eq. 5) into Eq.14 and integrating results in

$$\overline{\sigma_{y1}} \approx \sum_{n,l,m} c_{l,m}^{n\,*} \left[\sigma_{y1} \right]_{l,m}^n \quad (15)$$

with

$$\left[\sigma_{y1} \right]_{l,m}^n = \tau_{CRSS} \int_{S^3} Z_{l,m}^{n\,*}(q) \left(\frac{1}{\max\limits_{\alpha} \left| b_1^\alpha(q)\, n_1^\alpha(q) \right|} \right) \mathrm{d}q \quad (16)$$

In deriving Eq. 15 we have made use of the fact that an ODF is a real-valued function and is therefore equal to its complex conjugate, which allows us to exploit the orthogonality of the hyperspherical harmonic basis functions.

The form of Eq. 15 is significant. In this expression the microstructural information, as encoded in the ODF coefficients $c_{l,m}^n$, has been decoupled from the details of the physics, as encoded in the properties coefficients $\left[\sigma_{y1} \right]_{l,m}^n$. The use of this spectral framework permits such a decoupling and facilitates the fast computation of the effective properties [21], in this case $\overline{\sigma_{y1}}$. This is because the properties coefficients $\left[\sigma_{y1} \right]_{l,m}^n$ only have to be computed once, and then $\overline{\sigma_{y1}}$ may be evaluated for any microstructure ($c_{l,m}^n$) using the computationally efficient inner-product operation embodied in Eq. 15.

5.2. Elastic Compliance

The Voigt isostrain model [22, 23] for the effective elastic behavior of polycrystalline materials does not satisfy equilibrium constraints, but permits the derivation of a simple estimate for the relevant constants of the elastic compliance tensor. This estimate is an upper-bound and, for the specific case at hand, can be expressed as:

$$\overline{S_{1111}} = \int_{S^3} f(q)\, S_{1111}(q)\, \mathrm{d}q \quad (17)$$

4

S_{1111}	S_{1122}	S_{1212}
15.851	−5.7285	35.286

Table 1: Numerical values of the independent elastic constants for Al [24] appearing in Eq. 18. All values are in units of $10^{-12}\ Pa^{-1}$.

where the orientation dependent function $S_{1111}(q)$ is defined by

$$S_{1111}(q) = Q_{1a}(q)\,Q_{1b}(q)\,Q_{1c}(q)\,Q_{1d}(q)\,S_{abcd} \quad (18)$$

with $Q_{ij}(q)$ being one of the components of a direction cosine matrix and the Einstein summation convention implied for repeated indices. Eq. 18 may be evaluated in closed form, but it is lengthy and will be omitted here. Its evaluation requires the values of the independent single crystal elastic constants, which are provided in Table 1 for Al.

Again expressing the ODF appearing in Eq. 17 in spectral form, and integrating we arrive at a spectral expression for the Voigt estimate of the elastic compliance of a polycrystal:

$$\overline{S_{1111}} = \sum_{n,l,m} c_{l,m}^{n\,*}\,[s_{1111}]_{l,m}^{n} \quad (19)$$

with

$$[s_{1111}]_{l,m}^{n} = \int_{S^3} Z_{l,m}^{n\,*}(q)\,S_{1111}(q)\,\mathrm{d}q \quad (20)$$

Formally, the Fourier representation consists of an infinite series, but in all practical applications truncation is applied. In this work we include all terms through $n = 20$ for computation of both yield strength and elastic compliance.

5.3. Grain Boundary Network Diffusivity

Equations 15 and 19 represent spectral versions of existing texture sensitive models for initial plastic yield and elastic compliance, respectively. While texture sensitive models for many material properties exist, constitutive models that incorporate the influence of grain boundary network structure on the effective properties of polycrystalline materials are far fewer. Building on the work of Chen [25] and Frary [26] we construct a model for the effective diffusivity of polycrystals that depends on the structure of the grain boundary network and demonstrate how it too may be expressed in spectral form with the aid of the TJDF.

The diffusivities of individual grain boundaries can differ by orders of magnitude, leading to a sudden transition in the effective diffusivity of the grain boundary network as the distribution of grain boundary types changes, from a low-diffusivity regime to a high-diffusivity regime. This strong property contrast precludes the use of simple composite averaging or effective medium theory (EMT) models, which fail to capture this rapid "phase change" behavior [27]. Such systems are often better modeled using the tools of percolation theory. McLachlan proposed a phenomenological percolation theory based model for the effective electrical conductivity of binary mixtures of insulating and conducting phases [28, 29], which was adapted to the analogous case of grain boundary network diffusivity by Chen and Schuh [25]:

$$p_1 \frac{D_1^{1/s} - \left(2\overline{D}\right)^{1/s}}{D_1^{1/s} + \left(p_{c,2}^{-1} - 1\right)\left(2\overline{D}\right)^{1/s}} +$$

$$p_2 \frac{D_2^{1/t} - \left(2\overline{D}\right)^{1/t}}{D_2^{1/t} + \left(p_{c,2}^{-1} - 1\right)\left(2\overline{D}\right)^{1/t}} = 0 \quad (21)$$

In this expression p_1 and p_2 are the fraction of low- and high-angle grain boundaries, respectively, and $D_1 \leq D_2$ are the corresponding diffusivities. The exponents are constants that depend only on the dimensionality of the problem[1] and in this work are taken as $s = 1.09$ and $t = 1.13$. The spatial distribution of low- and high-angle grain boundaries in real materials is manifestly non-random and the percolation threshold for high-angle grain boundaries, $p_{c,2}$, is sensitive to these correlations in the grain boundary network [30, 31], which result from crystallographic constraints, texture, etc. These correlations have been observed to be short-range [32] and can be quantified by the triple junction fractions, $\{J_i \mid i \in [0, 3]\}$, which measure the fraction of triple junctions coordinated by i "special" grain boundaries (low-angle in the present context). Frary and Schuh found an empirical relation that predicts the percolation threshold[2] as a function of the J_i [26], the details of which will not be reproduced here for the sake of brevity, but which allows us to write $p_{c,2} = p_{c,2}(J_0, J_1, J_2, J_3)$.

The J_i can be interpreted as the average probability of observing a triple junction coordinated by

---

[1]See [25] for a brief discussion of this "universality hypothesis" for critical exponents in percolation theory.

[2]The expressions given in [26] were for $p_{c,1}$, but can be used to obtain $p_{c,2}$ by simply replacing Eq. 7b of [26] with its reciprocal.

i "special" grain boundaries in a given microstructure. Considering low-angle grain boundaries as "special", this interpretation allows us to compute the J_i by integration of the TJDF (Eqs. 7 or 8) according to:

$$J_i = \int_{\Omega_i} T(q_{12}, q_{23}) \, d\Omega_i \tag{22}$$

In Eq. 22, the domain $\Omega_i \subset S^3 \times S^3$ is the respective integration region defined by:

$$\Omega_0 = \{(q_{12}, q_{23}) \mid \hat{\omega}_{12} > \omega_t, \ \hat{\omega}_{23} > \omega_t, \ \hat{\omega}_{31} > \omega_t\} \tag{23a}$$

$$\begin{aligned}
\Omega_1 = {} & \{(q_{12}, q_{23}) \mid \hat{\omega}_{12} \leq \omega_t, \ \hat{\omega}_{23} > \omega_t, \ \hat{\omega}_{31} > \omega_t\} \\
& \cup \{(q_{12}, q_{23}) \mid \hat{\omega}_{12} > \omega_t, \ \hat{\omega}_{23} \leq \omega_t, \ \hat{\omega}_{31} > \omega_t\} \\
& \cup \{(q_{12}, q_{23}) \mid \hat{\omega}_{12} > \omega_t, \ \hat{\omega}_{23} > \omega_t, \ \hat{\omega}_{31} \leq \omega_t\}
\end{aligned} \tag{23b}$$

$$\begin{aligned}
\Omega_2 = {} & \{(q_{12}, q_{23}) \mid \hat{\omega}_{12} > \omega_t, \ \hat{\omega}_{23} \leq \omega_t, \ \hat{\omega}_{31} \leq \omega_t\} \\
& \cup \{(q_{12}, q_{23}) \mid \hat{\omega}_{12} \leq \omega_t, \ \hat{\omega}_{23} > \omega_t, \ \hat{\omega}_{31} \leq \omega_t\} \\
& \cup \{(q_{12}, q_{23}) \mid \hat{\omega}_{12} \leq \omega_t, \ \hat{\omega}_{23} \leq \omega_t, \ \hat{\omega}_{31} > \omega_t\}
\end{aligned} \tag{23c}$$

$$\Omega_3 = \{(q_{12}, q_{23}) \mid \hat{\omega}_{12} \leq \omega_t, \ \hat{\omega}_{23} \leq \omega_t, \ \hat{\omega}_{31} \leq \omega_t\} \tag{23d}$$

where ω_t is the angular threshold between low- and high-angle grain boundaries, which, based on diffusivity data for Al [33, pg. 122], we estimate to be $\omega_t = 20°$. In Eq. 23, $\hat{\omega}_{ij}$ is the rotation angle of the disorientation $\hat{q}_{ij}(\hat{\omega}_{ij}, \hat{\theta}_{ij}, \hat{\phi}_{ij})$ corresponding to the misorientation $q_{ij}(\omega_{ij}, \theta_{ij}, \phi_{ij})$. The disorientation, $\hat{q}_{ij}$, is the unique misorientation from among all of those symmetrically equivalent to q_{ij} that (1) has the smallest rotation angle, ω_{12}, and (2) has a rotation axis lying in the standard stereographic triangle. Uniqueness is guaranteed by enforcing the supplementary conditions for "reduced rotations" given by [34].

Introducing Eq. 7 into Eq. 22 and integrating we obtain

$$J_i = \sum_{\substack{n_1, \lambda_{12}, \mu_{12} \\ n_3, \lambda_{23}, \mu_{23}}} t^{n_3, \lambda_{23}, \mu_{23}}_{n_1, \lambda_{12}, \mu_{12}} [J_i]^{n_3, \lambda_{23}, \mu_{23}}_{n_1, \lambda_{12}, \mu_{12}} \tag{24}$$

where the term $[J_i]^{n_3, \lambda_{23}, \mu_{23}}_{n_1, \lambda_{12}, \mu_{12}}$ may be pre-computed, and is defined by

$$[J_i]^{n_3, \lambda_{23}, \mu_{23}}_{n_1, \lambda_{12}, \mu_{12}} = \int_{\Omega_i} Z^{n_1}_{\lambda_{12}, \mu_{12}}(q_{12}) \, Z^{n_3}_{\lambda_{23}, \mu_{23}}(q_{23}) \, d\Omega_i \tag{25}$$

In all practical situations the infinite series in Eqs. 7 and 24 will be truncated to some finite number of terms. Because of the harmonic nature of the basis functions, this can result in non-negligible truncation error when employing Eqs. 24 and 25, even giving non-physical negative values for the J_i on occasion. This problem is resolved by instead employing the Dirac basis representation of the TJDF (Eq. 8), which yields

$$J_i = \sum_{k=1}^{K} p_k [J_i]_k \tag{26}$$

The coefficient $[J_i]_k$ in the Dirac basis represents the triple junction fraction corresponding to $\left({}^k q_{12}, {}^k q_{23}\right)$, the k-th fundamental triple junction. This observation facilitates the efficient computation of the J_i simply by characterizing the number of "special" boundaries coordinating each of the fundamental triple junctions. To illustrate this idea let $\left({}^k q_{12}, {}^k q_{23}\right)$ be the k-th fundamental triple junction. If ${}^k\hat{\omega}_{12} < \omega_t$, ${}^k\hat{\omega}_{23} < \omega_t$, and ${}^k\hat{\omega}_{31} < \omega_t$ then $\left({}^k q_{12}, {}^k q_{23}\right)$ has all low-angle grain boundaries and is a J_3-type triple junction. We, therefore, have $[J_0]_k = 0$, $[J_1]_k = 0$, $[J_2]_k = 0$, and $[J_3]_k = 1$. Thus, the $[J_i]_k$ take the values 0 or 1 and may be computed directly, without the aid of Eq. 25 and its problematic integration, simply by characterizing the triple junction types of the fundamental triple junctions, which need only be performed once. The J_i for any microstructure can then be computed using Eq. 26, which simply represents a weighted average of the $[J_i]_k$ with the TJDF coefficients, p_k, providing the weights.

Introducing Eq. 26 into Frary's relation, $p_{c,2} = p_{c,2}(J_0, J_1, J_2, J_3)$, and recalling that $p_2 \approx 1 - \frac{1}{3}J_1 - \frac{2}{3}J_2 - J_3$ (see [35]), allows us to express all of the relevant microstructural parameters of our constitutive model for effective grain boundary network diffusivity (Eq. 21) in terms of the coefficients of the TJDF. By numerically solving the implicit equation represented by Eq. 21, we can express the effective grain boundary network diffusivity in a similar fashion to what we did for yield strength (Eq. 15) and compliance (Eq. 19): in spectral form as a function of the local properties (D_1 and D_2) and the microstructure (the Dirac TJDF coefficients p_k), according to

$$\overline{D} = \overline{D}(p_k, D_1, D_2) \tag{27}$$

For pure Al, we use $D_2 = 10^{-12} \ m^2/s$, which we estimate from the maximum calculated grain boundary diffusivity for $\langle 001 \rangle$ tilt grain boundaries at $250°C$ with diffusion perpendicular to $\langle 001 \rangle$ [36].

For the low-angle diffusivity we extrapolated the data in [36] to a tilt angle of $\theta = 0°$ to find $D_1 \approx 4.6 \times 10^{-20} \ m^2/s$.

We note that while this constitutive model employs the binary low-angle vs. high-angle grain boundary taxonomy, this is not essential to the design framework presented here and, given a suitable constitutive model, the full spectrum of grain boundary types can be considered.

6. Properties Closure

With constitutive models for the materials properties relevant to our design problem, expressed in spectral form, we are now in a position to define the properties closure [8]. Consider a space in which a microstructure is represented by a point, whose coordinates, $\left(\overline{\sigma_{y1}}, \overline{S_{1111}}, \overline{D}\right)$, indicate its materials properties. The properties closure is the closed region in this space containing all physically possible combinations of these three properties. It can be defined mathematically by

$$\mathscr{P} = \left\{ \left(\overline{\sigma_{y1}}, \overline{S_{1111}}, \overline{D}\right) \middle| \overline{\sigma_{y1}} = \sum_{n,l,m} c_{l,m}^{n*} \left[\sigma_{y1}\right]_{l,m}^{n}, \right.$$
$$\overline{S_{1111}} = \sum_{n,l,m} c_{l,m}^{n*} [s_{1111}]_{l,m}^{n}, \ \overline{D} = \overline{D}(p_k, D_1, D_2),$$
$$\left. \left\{c_{l,m}^{n}\right\} \in m_H^{(1)}, \{p_k\} \in \widetilde{M}_H^{(3)}, \left\{c_{l,m}^{n}\right\} \to \{p_k\} \right\}$$
(28)

where $m_H^{(1)}$ and $\widetilde{M}_H^{(3)}$ are microstructure hulls [6, 8]—specifically, the texture hull in the Fourier basis, and the uncorrelated triple junction hull in the Dirac basis, respectively. The last expression, $\left\{c_{l,m}^{n}\right\} \to \{p_k\}$, indicates a relationship between the ODF and TJDF coefficients that is a result of a mapping from $m_H^{(1)} \leftarrow M_H^{(1)} \to \widetilde{M}_H^{(3)}$, that will be defined below. As the microstructure hull contains all possible microstructural configurations, the properties closure is constructed by exercising our structure-property models (Eqs. 15, 19, and 27) over the entirety of the appropriate microstructure hull. While this is conceptually straightforward—if you compute the properties over the space of all possible microstructures you will obtain the space of all possible properties—in practice it involves a number of steps:

Step 1: Sample ODFs from $M_H^{(1)}$
Step 2: Map from $M_H^{(1)} \to m_H^{(1)}$

Step 3: Compute texture dependent properties: $\overline{\sigma_{y1}}$ and $\overline{S_{1111}}$
Step 4: Map from $M_H^{(1)} \to \widetilde{M}_H^{(3)}$ to obtain the TJDF corresponding to each ODF
Step 5: Compute grain boundary network sensitive properties: $\overline{D}$
Step 6: Define the boundary of $\mathscr{P}$

This process is graphically summarized in Fig. 1. In what follows, each of these steps will be explained in detail.
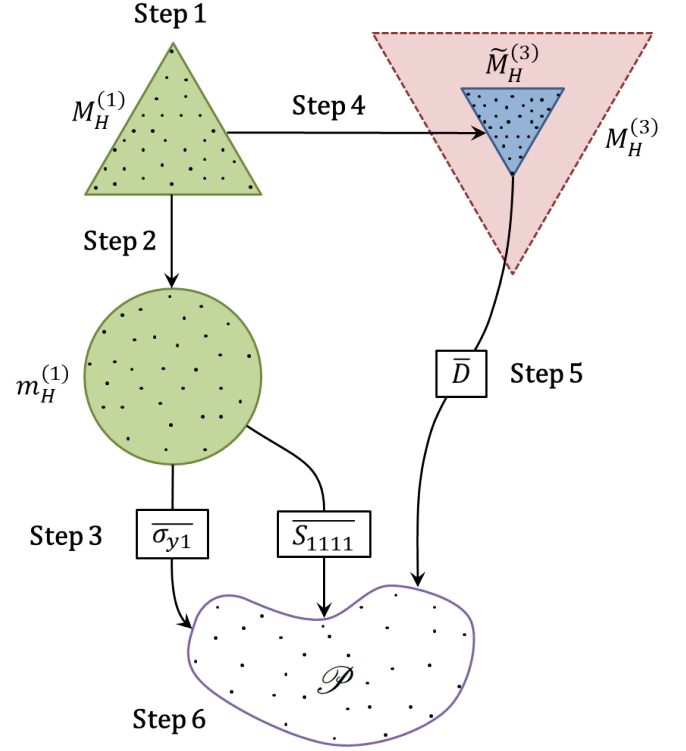

Fig. 1: Graphical summary of the process of constructing the properties closure.

6.1. Step 1: Sample ODFs from $M_H^{(1)}$

To construct the properties closure, we take a stochastic approach and sample many microstructures from the appropriate microstructure hull, compute the relevant material properties of each, and define $\mathscr{P}$ as the region in property space that bounds all of the resulting points.

There are two microstructure hulls relevant to the present design problem: $\mathscr{M}_H^{(1)}$ and $\widetilde{\mathscr{M}}_H^{(3)}$. Johnson & Schuh derived a formula that permits the computation of the TJDF coefficients in the Fourier basis from those of an ODF when spatial correlations in grain orientation are absent [6]. For reasons that will be explained below, we require an equivalent formula in the Dirac basis, which we will derive in Section 6.4. These relationships effectively provide a mapping between $\mathscr{M}_H^{(1)}$ and $\widetilde{\mathscr{M}}_H^{(3)}$. In light

of this, we choose to sample from $\mathscr{M}_H^{(1)}$ and subsequently map these points to $\widetilde{\mathscr{M}}_H^{(3)}$.

Because our texture dependent constitutive relations are formulated in the Fourier basis it seems natural to sample ODFs from $m_H^{(1)}$. The texture hull, $m_H^{(1)}$, is defined as the convex hull of the texture set, $m_S^{(1)}$. For all practical purposes $m_S^{(1)}$ will be finite, consequently, $m_H^{(1)}$ will be a convex polytope, which can be sampled uniformly using a *hit-and-run* algorithm as discussed in [6]. However, there is a major drawback to this method. To sample from $m_H^{(1)}$ you must explicitly define its boundary, which requires the computation of a convex hull. Constitutive equations for all but the simplest properties can require a large number of coefficients, $c_{l,m}^n$, and consequently $m_H^{(1)}$ will exist in a high-dimensional space. The computational cost of constructing a convex hull scales exponentially with the dimension [37], making this approach too computationally expensive for practical use.

In the Dirac basis the texture hull, $M_H^{(1)}$, has a far simpler geometry: it is the standard $(J-1)$-simplex, where J is the cardinality of $M_S^{(1)}$. This fact obviates the need to explicitly compute a convex hull, and also makes the procedure for sampling far simpler. Sampling uniformly from a standard $(J-1)$-simplex can be accomplished by standard methods; however, regardless of the basis, uniform sampling of microstructure hulls is known to result in poor sampling of the corresponding properties closure [8], with all of the points clustered near its center (see Fig. 2). The cause of this phenomenon stems from the fact that extremal properties are generally exhibited by extremal microstructures, which reside on the surface of the microstructure hull. However, the dimensionality of the surface of the microstructure hull is one less than that of its volume and consequently it has measure 0 and is never sampled if uniform sampling is employed.

We have recently devised an alternate method called *hierarchical simplex sampling* (HSS) [38] that leverages the geometric structure of microstructure hulls in the Dirac basis to efficiently generate samples in both the interior and covering the surface of the microstructure hull in such a way that the resulting points span the properties closure. Figure 2 illustrates the improved performance of HSS for a two-dimensional properties closure consisting of the texture sensitive properties for the present design problem. For the present

design problem we use this HSS algorithm to sample $N_S = 10^8$ textures from $M_S^{(1)}$. We will denote this set of sampled textures

$$\mathcal{S} = \left\{ \boldsymbol{p}'_s \mid \boldsymbol{p}'_s = \left\{ p'_j \right\}_s, \ j \in [1, J], \ s \in [1, N_S] \right\} \quad (29)$$

where $\boldsymbol{p}'_s$ is the s-th sample, and can be interpreted as a vector of coefficients $\left\{ p'_j \right\}_s = \left(p'_1, p'_2, \ldots, p'_J \right)^T$. In this way $\mathcal{S}$, which is a set of sets, can be represented as a matrix where $\mathcal{S}_{js}$ is the j-th coefficient of the s-th sample.
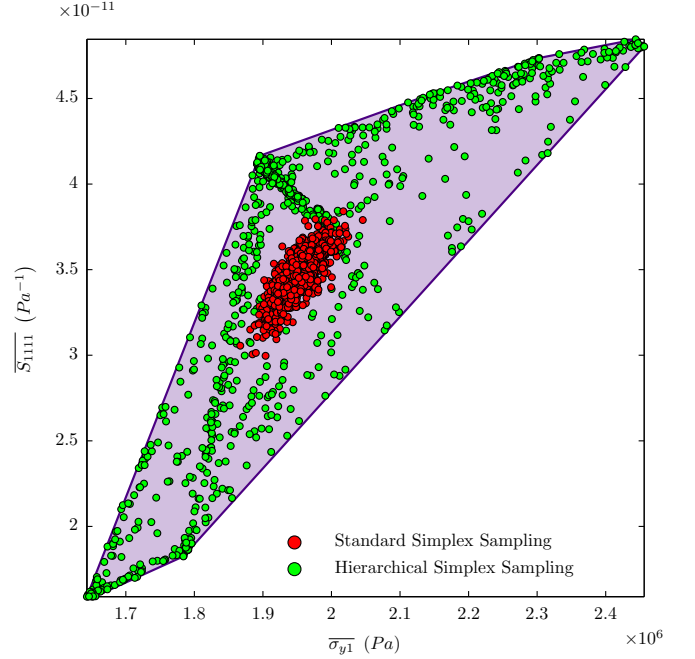

Fig. 2: Comparison of microstructural sampling techniques for $N_S = 10^3$. Points resulting from uniform sampling of the standard simplex are shown as red markers. Points resulting from the hierarchical simplex sampling technique are shown as green markers. The purple shaded region is the convex hull of 10^5 samples taken using the hierarchical technique and is shown for comparison, being a higher order approximation of the true $\mathscr{P}\left(\overline{\sigma_{y1}}, \overline{S_{1111}} \right)$, for the texture dependent properties $\overline{\sigma_{y1}}$, and $\overline{S_{1111}}$.

6.2. Step 2: Map from $M_H^{(1)} \to m_H^{(1)}$

Because we sampled texture coefficients, p'_j, in the Dirac basis and our models for $\overline{\sigma_{y1}}$, and $\overline{S_{1111}}$ are in the Fourier basis, we must perform a transformation $M_H^{(1)} \to m_H^{(1)}$ in order to obtain the Fourier texture coefficients $c_{l,m}^n$ that our models require. This transformation is accomplished by taking the generalized Fourier transform of Eq. 6, yielding the following formula:

$$c_{l,m}^n = \sum_{j=1}^{J} p'_j \, {}^j c_{l,m}^n \quad (30)$$

8

which is the texture analog to Eq. 12 of [6], originally developed for the TJDF coefficients. In Eq. 30, the $^{j}\left\{c_{l,m}^{n}\right\} \in m_{S}^{(1)}$ are the Fourier coefficients of the j-th element of the texture set (see Eq. 9).

6.3. Step 3: Compute texture dependent properties

With Dirac ODF coefficients sampled and transformed to the Fourier basis, the texture dependent properties can now be directly evaluated for each sampled texture by means of Eqs. 15 and 19. For each texture we now have the two coordinates $\left(\overline{\sigma_{y1}}, \overline{S_{1111}}\right)$ in property space that are shown in Fig. 2.

6.4. Step 4: Map from $M_{H}^{(1)} \rightarrow \widetilde{M}_{H}^{(3)}$

In the present design problem we are using texture dependent constitutive equations for $\overline{\sigma_{y1}}$ and $\overline{S_{1111}}$, and a grain boundary network sensitive model for $\overline{D}$. To construct a properties closure that is self-consistent, we must, therefore, be able to identify the grain boundary network configuration corresponding to a given texture.

In general the mapping between texture and grain boundary network configuration, $\mathscr{M}_{H}^{(1)} \rightarrow \mathscr{M}_{H}^{(3)}$, is many-to-many. For a given texture, different spatial arrangements of the grains will result in distinct grain boundary network configurations (TJDFs). Likewise, a given grain boundary network configuration may be obtained from many different textures. For example, all textures that differ only by a rotation, r, $e.g.$ $f(q)$ and $f(qr)$, will yield the same TJDF (this also implies that, given a TJDF, it is only possible to recover the corresponding ODF modulo a rotation operation) [39]. However, under the assumption that grain orientations are spatially uncorrelated we obtain the mapping $\mathscr{M}_{H}^{(1)} \rightarrow \widetilde{\mathscr{M}}_{H}^{(3)}$, for which every ODF maps to only one TJDF. Taking advantage of this fact, we can take the texture coefficients, p_{j}', sampled from $M_{H}^{(1)}$ and map them to $\widetilde{M}_{H}^{(3)}$ to obtain the corresponding TJDF coefficients, $\widetilde{p}_{k}$. A formula for this mapping, developed in the context of the Fourier basis, was given in [6]. In the Dirac basis, this mapping takes a particularly simple form and is given by [39]:

$$\widetilde{p}_{k} = \sum_{(a,b,c)\in E_{k}} p_{a}' p_{b}' p_{c}' \tag{31}$$

While simple in form, Eq. 31 deserves some explanation. The triple junction set, $M_{S}^{(3)}$, effectively discretizes the triple junction space. The probability of observing a triple junction associated with

the k-th fundamental triple junction in a given microstructure is given by p_{k}. Eq. 31 says that, in the absence of spatial correlations in grain orientation, this probability is given by the joint probability of observing the triplet of grain orientations (q_{a}, q_{b}, q_{c}) summed over all grain orientation triplets belonging to the equivalence class of $\left({}^{k}q_{12}, {}^{k}q_{23}\right)$, denoted by E_{k}. The equivalence class E_{k} is defined by the equivalence relations induced by both crystallographic symmetry and triple junction symmetry. The equivalence relations for triple junction symmetry were defined in [6], and are reproduced here:

$$F = \left\{ [q_{12}, q_{23}], \left[q_{23}, q_{23}^{-1}q_{12}^{-1}\right], \left[q_{23}^{-1}q_{12}^{-1}, q_{12}\right], \\ \left[q_{12}^{-1}, q_{12}q_{23}\right], \left[q_{12}q_{23}, q_{23}^{-1}\right], \left[q_{23}^{-1}, q_{12}^{-1}\right] \right\} \tag{32}$$

where $[a, b] \equiv \{(q_{12}, q_{23}) \mid (q_{12}, q_{23}) \sim (a, b)\}$.

While, strictly speaking, $\mathscr{M}_{S}^{(1)}$ and $\mathscr{M}_{S}^{(3)}$ may be defined independently of one another, the use of Eq. 31 is computationally facilitated by constructing them in such a way that they are related. Specifically, we begin by defining $\mathscr{M}_{S}^{(1)}$ by the crystal orientations $\left\{{}^{1}q, {}^{2}q, \ldots, {}^{J}q\right\}$ where J is the cardinality of $\mathscr{M}_{S}^{(1)}$ and defines its resolution. For the present design problem we defined $\mathscr{M}_{S}^{(1)}$ using a multilevel pseudo-grid over the cubic fundamental zone composed of 10 regularly spaced primary orientations each with 6 secondary orientations being defined as rotations of $9°$ along the six $\langle 100 \rangle$-type axes relative to the respective primary orientation. Thus, for the present design problem we have $J = 70$. Figure 3 shows the structure of this pseudo-grid in the cubic fundamental zone. These same orientations are shown in their pole figure representation in Fig. 4.

With the fundamental orientations defined, we can identify all possible triple junctions that can be constructed therefrom. A triple junction may be defined by the ordered triplet of orientations coordinating it: $\left({}^{a}q_{1}, {}^{b}q_{2}, {}^{c}q_{3}\right)$, where the superscripts are an index into the set of fundamental orientations, and the subscripts denote the grain to which the orientation belongs. The set of all possible triple junctions that can be constructed from the set of the fundamental orientations is given by

$$\left\{ \left({}^{1}q_{1}, {}^{1}q_{2}, {}^{1}q_{3}\right), \left({}^{1}q_{1}, {}^{1}q_{2}, {}^{2}q_{3}\right), \ldots, \\ \left({}^{1}q_{1}, {}^{2}q_{2}, {}^{3}q_{3}\right), \ldots, \left({}^{J}q_{1}, {}^{J}q_{2}, {}^{J}q_{3}\right) \right\} \tag{33}$$

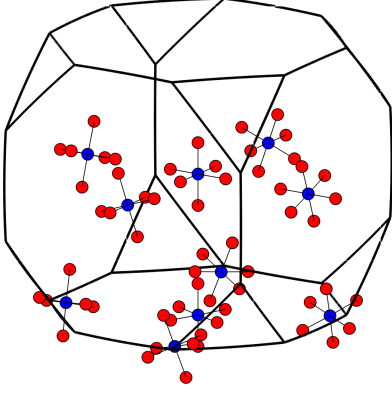which has cardinality J^{3}. This can then be ex-

Fig. 3: Multilevel pseudo-grid over the cubic fundamental zone (FZ) shown using the quaternion parameterization and an isovolumetric projection [13] to three-dimensions. Blue markers indicate the primary orientations and red markers indicate the secondary orientations. Lines connecting secondary orientations to their respective primary orientations are also shown. Several orientations are located outside of the FZ and would normally be represented by their symmetric image inside of the FZ, but they are plotted as shown to highlight the structure of the pseudo-grid
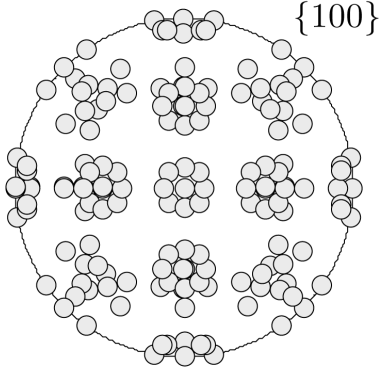
Fig. 4: A {100} pole figure showing the orientations used to define $\mathscr{M}_S^{(1)}$.

pressed in terms of misorientations according to

$$\left\{ \left({}^{(1,1)}q_{12}, {}^{(1,1)}q_{23} \right), \left({}^{(1,1)}q_{12}, {}^{(1,2)}q_{23} \right), \ldots, \right.$$
$$\left. \left({}^{(1,2)}q_{12}, {}^{(2,3)}q_{23} \right), \ldots, \left({}^{(J,J)}q_{12}, {}^{(J,J)}q_{23} \right) \right\} \quad (34)$$

where ${}^{(a,b)}q_{12}$ denotes a misorientation between the first and second grains coordinating a triple junction, respectively possessing orientations corresponding to the a-th and b-th elements of the set of fundamental orientations. Let $\mathscr{C}$ denote a crystallographic point group, and $c_i \in \mathscr{C}$ one of the rotational symmetry operators belonging to $\mathscr{C}$. Crystallographic symmetry induces equivalence relations on orientations according to $q \sim qc_i \; \forall \; c_i \in \mathscr{C}$. We denote the set of all such equivalence relations by C. In addition to crystallographic symmetry there are distinct triple junction symmetries as described in [6, 39], which induce triple junction equivalence relations. The set of all triple junc-

tion equivalence relations was given explicitly by Eq. 32 and is denoted by F. We next find the K equivalence classes, $\{E_k \mid k \in [1, K]\}$, of Eq. 34 that are induced by the combined application of C and F. From each E_k we select one unique representative and denote it $\left({}^k q_{12}, {}^k q_{23} \right)$ and this becomes the k-th fundamental triple junction, which is subsequently used to define $\mathscr{M}_S^{(3)}$. In this way $\mathscr{M}_S^{(3)}$ is composed of the unique triple junctions that may be constructed exclusively from the fundamental orientations that define $\mathscr{M}_S^{(1)}$. Having constructed $\mathscr{M}_S^{(3)}$ in this way, we already have the E_k necessary to evaluate Eq. 31, and thereby compute the TJDF coefficients corresponding to a given ODF in the Dirac basis. Employing this approach we obtain 6,411 fundamental triple junctions from the 70 fundamental orientations.

The motivation behind the multilevel pseudo-grid used to construct the set of fundamental orientations stems from the fact that the portions of the triple junction character space belonging to each triple junction type (J_0, J_1, J_2, and J_3) are not equal in size, making certain types of triple junctions, J_2 in particular, relatively rare as a result of crystallogrpahic constraints. At the same time, J_2 type triple junctions are experimentally observed [31], and can play a critical role in determining GBN connectivity as they are the *only* types of triple junctions at which non-closed connected paths of high-diffusivity GBs can terminate. Consequently, a set of fundamental triple junctions that omits J_2 type triple junctions would significantly and unnaturally restrict the GBN configurations that could be considered. Since the fundamental triple junctions were derived from the fundamental orientations, it was necessary to construct the set of fundamental orientations in such a way that each type of triple junction appeared in the resulting set of fundamental triple junctions (though, not necessarily with equal frequency as shown in Table 2). The resolution of a regular discretization of orientation space necessary to produce triple junctions of type 2 is prohibitively high; therefore, the multilevel pseudo-grid approach was employed to provide representation of all 4 triple junction types with fewer discretization points.

6.5. Step 5: Compute grain boundary network properties

Using Eq. 31 we can now find the TJDF coefficients in the Dirac basis for each of the textures sampled from $M_H^{(1)}$. Using Eq. 27 the grain bound-

J_0	J_1	J_2	J_3
0.7029	0.2884	0.0022	0.0066

Table 2: Fraction of each triple junction type appearing in the set of fundamental triple junctions resulting from the multi-level pseudo-grid discretization of orientation space. Only four significant figures are shown here, but we verified that using full precision $\sum_i J_i = 1$ to within machine epsilon.

ary network sensitive property $\overline{D}$ can then be determined for each sampled point and we obtain the triplet of property coordinates $\left(\overline{\sigma_{y1}}, \overline{S_{1111}}, \overline{D}\right)$. The property space coordinates of the sampled textures are shown in Fig. 5.
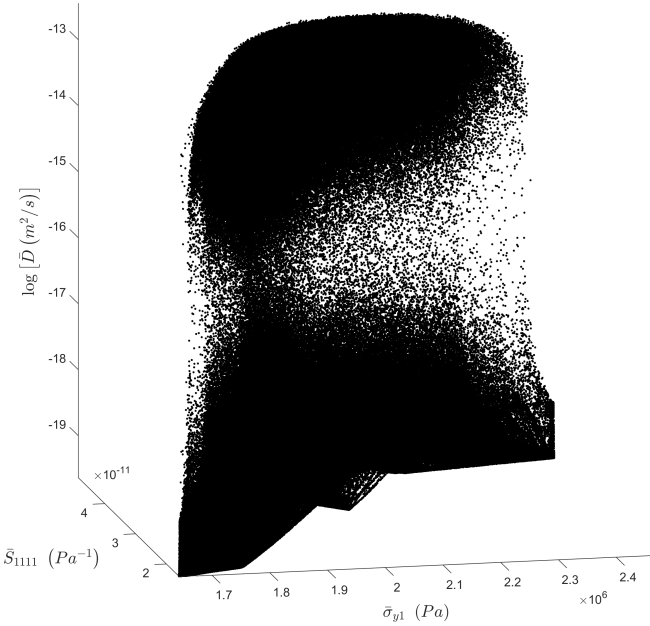
Fig. 5: Properties space representation of each of the sampled textures. Only 10^7 of the 10^8 points are shown.

6.6. Step 6: Define the boundary of $\mathscr{P}$

We wish to define $\mathscr{P}$, which is the envelope of all physically possible properties combinations under the assumptions of the constitutive models that we used and the condition of uncorrelated grain orientations. The convexity that is guaranteed for microstructure hulls, such as $\mathscr{M}_H^{(1)}$ and $\mathscr{M}_H^{(3)}$, does not extend to properties closures [8]. This is particularly true for properties closures involving nonlinear constitutive relations.

The general problem of defining the non-convex envelope of a set of points has no unique solution. A number of methods have been developed (see the review provided by [40] and references contained therein), each making certain assumptions that induce additional constraints necessary to define a solution. One method that is often employed,

and which we will use, is that of finding an α-shape [41, 42]. Let S be a set of points in $\mathbb{R}^3$. Consider a ball, B, of radius $\alpha \in [0, \infty)$. When $\alpha = 0$, B is a point, and as $\alpha \to \infty$ it becomes a half-space. The α-hull is defined as the region of $\mathbb{R}^3$ through which B cannot be translated without enclosing any of the points in S. To give a more intuitive picture, consider a region $R \subseteq \mathbb{R}^3$. Initially let $R = \mathbb{R}^3$ and imagine that B is translated throughout the entirety of $\mathbb{R}^3$. Anywhere that B can be placed without enclosing any points in S is removed from R. What remains of R after this exercise will be a closed, but not-necessarily convex or connected, region called the α-hull of S. By replacing the curved boundaries of the α-hull with flat planes, we recover the polytope referred to as the α-shape. The α shape is a generalization of the convex hull, and when $\alpha = \infty$ the convex hull is recovered. Fig. 6 shows α-shapes with various values of α for a two-dimensional point cloud.

Because the scales of $\overline{\sigma_{y1}}$, $\overline{S_{1111}}$, and $\overline{D}$ differ significantly, choosing an appropriate value of α for our design problem is difficult. To address this issue, the property coordinates were normalized for the purposes of the α-shape computation according to the following transformations:

$$x = \frac{2\overline{\sigma_{y1}} - \left(\max\left(\overline{\sigma_{y1}}\right) + \min\left(\overline{\sigma_{y1}}\right)\right)}{\max\left(\overline{\sigma_{y1}}\right) - \min\left(\overline{\sigma_{y1}}\right)} \quad (35a)$$

$$y = \frac{2\overline{S_{1111}} - \left(\max\left(\overline{S_{1111}}\right) + \min\left(\overline{S_{1111}}\right)\right)}{\max\left(\overline{S_{1111}}\right) - \min\left(\overline{S_{1111}}\right)}$$
$$(35b)$$

$$z = \frac{2\ln\overline{D} - \left(\max\left(\ln\overline{D}\right) + \min\left(\ln\overline{D}\right)\right)}{\max\left(\ln\overline{D}\right) - \min\left(\ln\overline{D}\right)} \quad (35c)$$

where $\max\left(\overline{\sigma_{y1}}\right)$ denotes the maximum observed value of $\overline{\sigma_{y1}}$ among all of the samples, and so on for the other properties. In the space of (x, y, z) a parameter value of $\alpha = 0.75$ was employed. Applying the α-shape algorithm to the normalized coordinates of the property space point cloud yields our desired result: delineation of the properties closure, $\mathscr{P}$, which is shown in Fig. 7. Note the non-convex regions of $\mathscr{P}$, particularly evident near the bottom.
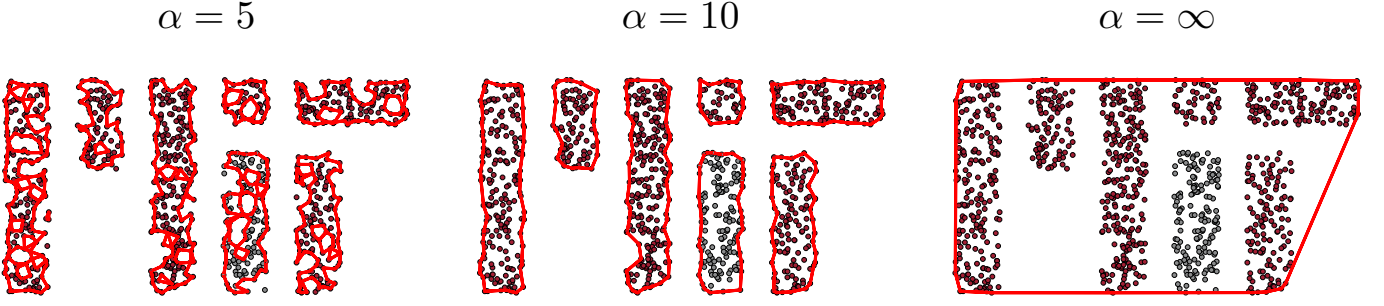
$$\alpha = 5 \qquad\qquad \alpha = 10 \qquad\qquad \alpha = \infty$$

Fig. 6: α-shapes for a point cloud with various values of the parameter α. The figure to the far right with $\alpha = \infty$ shows the convex hull of the point cloud.
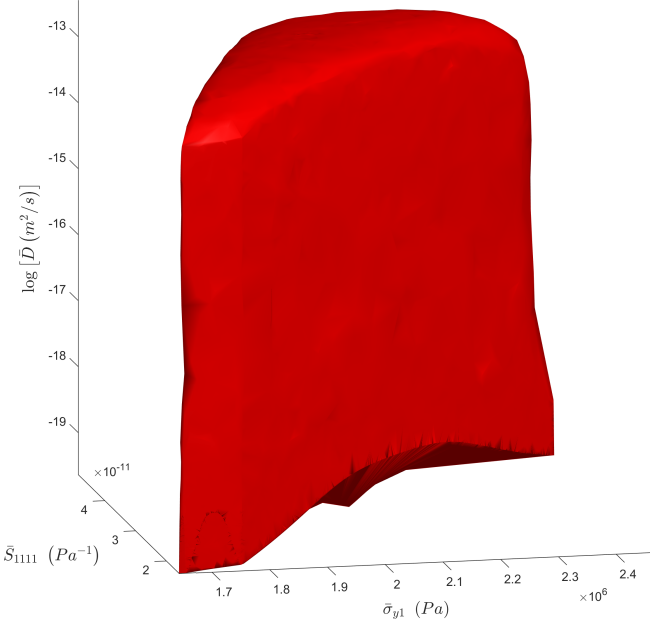

Fig. 7: The properties closure, $\mathscr{P}$, for the properties $\overline{\sigma_{y1}}$, $\overline{S_{1111}}$, and $\overline{D}$ as approximated using the procedures outlined in Section 6.
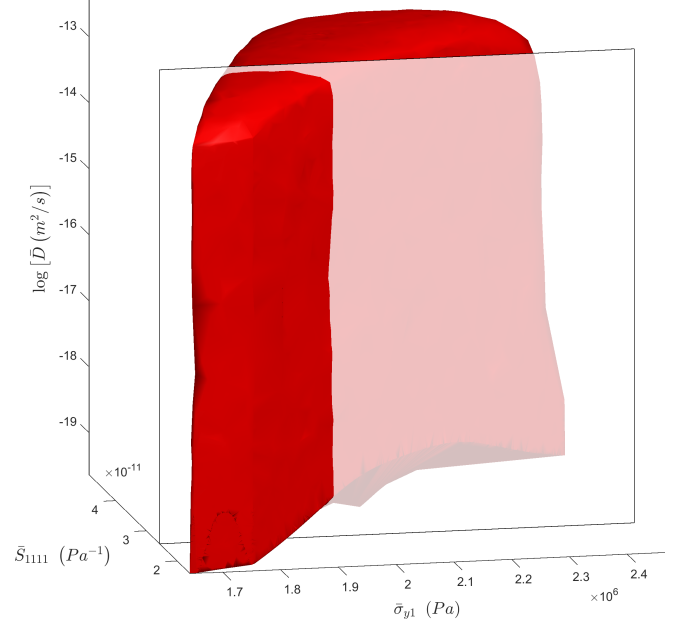

Fig. 8: Intersection of the design constraint $\overline{S_{1111}} = S_{1111}^{sub}$ with $\mathscr{P}$, for $S_{1111}^{sub} = 2.5665 \times 10^{-11}\ Pa^{-1}$. This design constraint is represented as the semi-transparent vertical plane.

7. Solving the Design Problem

The objectives of the present design problem were given in Eq. 1. The constraint $\overline{S_{1111}} = S_{1111}^{sub}$ given in Eq. 1b may be represented in the property space as a plane, as illustrated in Fig. 8, where we take $S_{1111}^{sub} = 2.5665 \times 10^{-11}\ Pa^{-1}$. The feasible region of our design problem lies on the intersection of this plane and $\mathscr{P}$, and is shown in Fig. 9. In order to satisfy Eqs. 1a and 1c, we can define a composite objective function to minimize:

$$f_{obj} = \frac{z + 2\,|z_{\min}|}{x + 2\,|x_{\min}|} \qquad (36)$$

where x and z are the normalized coordinates of $\overline{\sigma_{y1}}$ and $\overline{D}$, respectively, as defined in Eq. 35. The theoretical minimum values of $\overline{\sigma_{y1}}$ and $\overline{D}$ in the present context and considering 2D honeycomb GBNs are, respectively, $\left(\overline{\sigma_{y1}}\right)_{\min} = 2\tau_{CRSS}$ and $\left(\overline{D}\right)_{\min} = D_1/2$. The terms $x_{\min}$ and $z_{\min}$, appearing in Eq. 36, are the normalized coordinates of these values.

In the context of texture sensitive microstructure design, several methods have been used to search $\mathscr{P}$ for an optimal design solution including both gradient-based [43] and stochastic methods [44]. Since we have already sampled many microstructures to generate $\mathscr{P}$ we leverage this expended effort and take the solution to the design problem to be

$$\min_{S \in \mathscr{R}} f_{obj} \qquad (37)$$

where

$$\mathscr{R} = \left\{ \left(\overline{\sigma_{y1}}, \overline{S_{1111}}, \overline{D}\right) \,\middle|\, \frac{\left|\overline{S_{1111}} - S_{1111}^{sub}\right|}{\left(\overline{S_{1111}}\right)_{\max} - \left(\overline{S_{1111}}\right)_{\min}} < 10^{-6} \right\} \qquad (38)$$

is the region of properties space within some tolerance of the plane $\overline{S_{1111}} = 2.5665 \times 10^{-11}\ Pa^{-1}$.

In Fig. 9, the contours of f_{obj} are plotted over the feasible region. The optimal microstructure
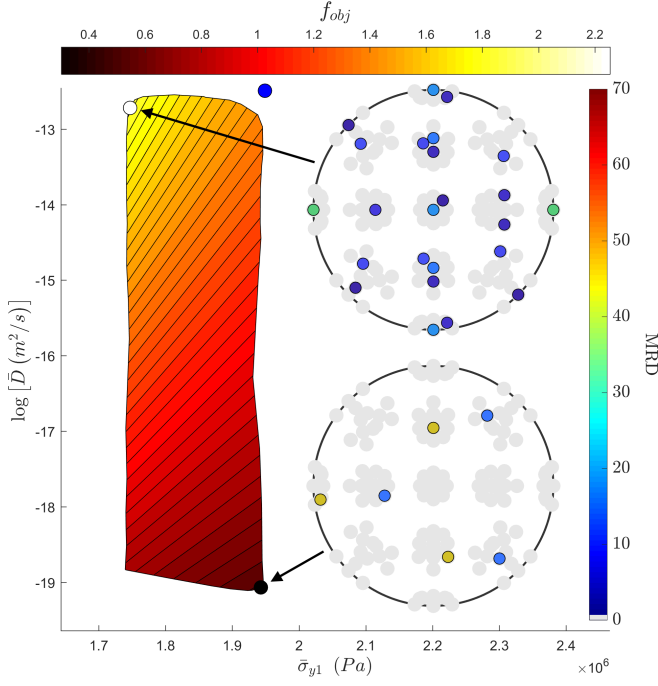
Fig. 9: The feasible region for the design problem. Contours of the objective function, f_{obj}, as defined in Eq. 36, are plotted over the feasible region. The best performing design solution is shown (black dot) along with the worst performing solution (white dot) and the isotropic solution (blue dot). The isotropic solution does not satisfy the design constraints and falls outside of the feasible region. The textures of the best and worst solutions are also shown as {100} pole figures where the gray discrete points are the fundamental orientations defining $M_S^{(1)}$. The color scale for the texture components is in multiples of the random distribution (MRD).

(black dot) lies at the bottom tip of the feasible region. The corresponding texture is composed of a roughly 75%/25% mixture of two orientations, the majority orientation being one with a very low yield strength ($\sigma_{y,1} = 1.8$ MPa) and the minority orientation having the largest yield strength from among the fundamental orientations ($\sigma_{y,1} = 2.5$ MPa). The worst performing microstructure has a texture that is reminiscent of a weak fiber texture with the shared rotation axis parallel to the loading direction. An isotropic microstructure possessing no texture (*i.e.* a uniform ODF) would not satisfy the design constraint on $\overline{S}_{1111}$, but it is also plotted in Fig. 9 for comparison as it exhibits the properties that might be expected for an "unde-signed" microstructure.

The TJDF coefficients corresponding to the textures shown in Fig. 9 were also obtained; however, since the TJDF is a six-dimensional function, its direct visualization is difficult. Instead, we have reconstructed simulated microstructures with hexagonal grains and assigned grain orientations in a spatially uncorrelated fashion from each of the respec-

tive ODFs. In Fig. 10 the grain boundary networks of each of these microstructures are shown with grain boundaries colored according to their disorientation using the Patala coloring scheme [45, 46], which encodes both the rotation angle and axis of the disorientation.

The crystallographic structure of the grain boundary networks is dramatically different. Most notably, the grain boundary networks of the isotropic and worst performing microstructures both contain a large diversity of grain boundary types, including many high-angle (D_2-type) grain boundaries. In contrast, the best performing microstructure is largely single crystal (GBs colored white correspond to a misorientation of 0°), and where GBs do exist they are exclusively of one type: a rotation of just over 50° about an axis close to $\langle 110 \rangle$.
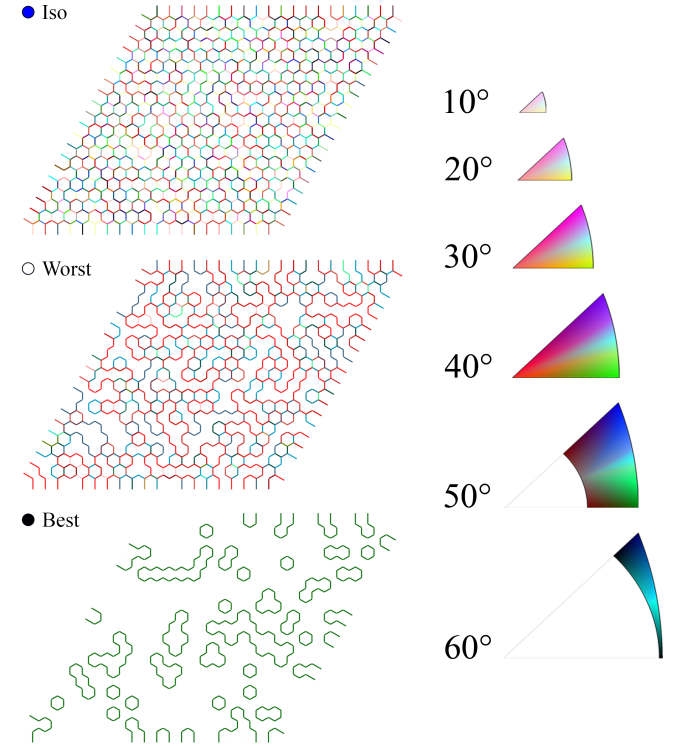

Fig. 10: The grain boundary networks corresponding to the best, worst, and isotropic design solutions shown in Fig. 9. Grain boundaries are colored by their disorientation angle and axis according to the Patala coloring scheme [45, 46]. For a given disorientation angle, the color code on the right indicates the corresponding rotation axis by its position in the relevant standard stereographic triangle.

The optimal microstructure outperforms the worst performing microstructure and the isotropic solution by over six orders of magnitude in terms of $\overline{D}$. Median time to failure (MTF) for electromigration is inversely proportional to an Arrhenius term involving the activation energy for atomic migration [11]. Since diffusivity is directly proportional

to this same Arrhenius term, we have that $MTF \propto (\overline{D})^{-1}$. Therefore, in terms of resistance to electromigration the optimal solution is expected to have a MTF that is roughly 3.8×10^6 times longer than that of an undesigned isotropic material. While the isotropic solution is predicted to exhibit a yield strength that is slightly higher than the optimal solution (by about 0.3%), it has a much higher diffusivity and therefore is significantly more vulnerable to electromigration failure. The optimal solution outperforms the yield strength of the worst solution by 11.2%. Although compared to the improvement in MTF this enhancement seems modest, the maximum possible yield strength in the feasible region is only a roughly 11.9% improvement over the worst solution, so the yield strength improvement of the best solution represents roughly 95% of what is theoretically possible.

Although the configuration of the optimal microstructure is consistent with one's intuition—a grain boundary network that maximizes the fraction of J_3-type triple junctions while maintaining polycrystallinity for the purposes of yield strength—further investigation reveals additional insights. The competition between yield strength and diffusivity leads to a microstructure consisting exclusively of J_1- and J_3-type triple junctions (See Fig. 11), which has important implications for grain boundary network topology. For instance, because there are no J_2-type triple junctions, all of the connected paths of high-diffusivity grain boundaries are closed loops and therefore percolation is avoided.

Frary showed that a pair of order parameters, $\sigma \in [-1, 1]$ and $\chi \in [-1, 1]$, can be defined for grain boundary networks in terms of the triple junction fractions [26]. σ characterizes the tendency for low-angle grain boundaries to mix ($\sigma < 0$) or segregate ($\sigma > 0$), while χ characterizes the tendency of low-angle grain boundaries to form compact ($\chi < 0$) or elongated ($\chi > 0$) clusters. Figure 12 presents the values of σ and χ for all of the microstructures in the feasible region. Microstructures located in the interior of the feasible region and near the optimal microstructure tend to have higher values of σ indicating that low-angle grain boundaries in these microstructures are strongly segregated. Comparison with Fig. 11 confirms that the optimal microstructure exhibits highly segregated clusters of low-angle grain boundaries, $\sigma_{\text{best}} = 0.46$, whereas the worst-performing microstructure exhibits a greater degree
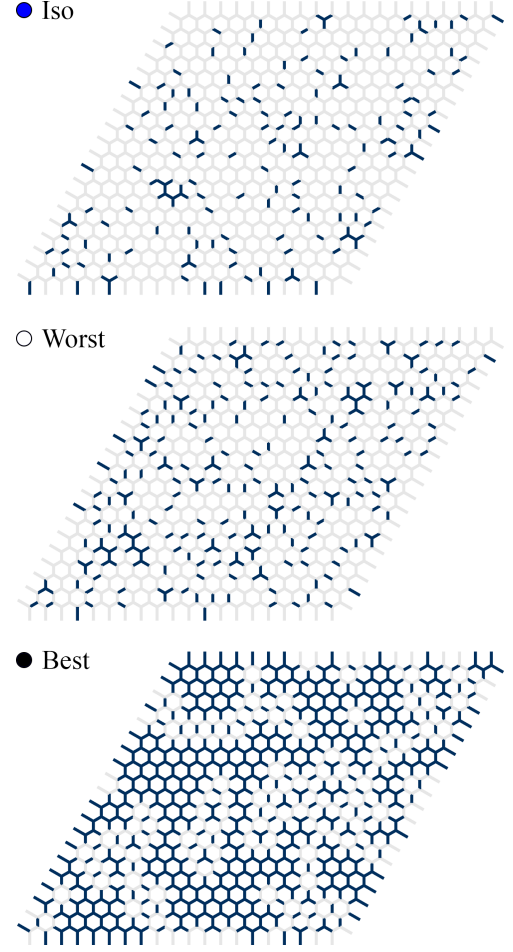

Fig. 11: The grain boundary networks corresponding to the best, worst, and isotropic design solutions shown in Fig. 9. Low-angle grain boundaries are colored dark blue and high-angle grain boundaries are colored light gray to highlight low-angle grain boundary segregation and cluster topology. Note that in this view the triple junction types are easily observed, e.g. triple junctions coordinated by three dark blue boundaries are J_3-type triple junctions.

of mixing $\sigma_{\text{worst}} = 0.1$. In contrast, there does not appear to be any clear correlation between χ and the performance of the microstructures—with most of the microstructures having $\chi \approx 1$. Thus it appears that, for the present design problem, the degree of segregation may be more important (or at least may more strongly differentiate the performance of different microstructures) than the topology of low-angle grain boundary clusters.

While the properties closure delineates the envelope of all theoretically possible properties combinations, it does not directly encode the likelihood of observing those microstructural states. Frary showed that the configurational entropy of a grain boundary network S_{config}, which is related to the likelihood of observing a particular configuration, can also be computed from the triple junction fractions [47]. A reference value, S_{config}^0, can be set by the maximum entropy configuration,
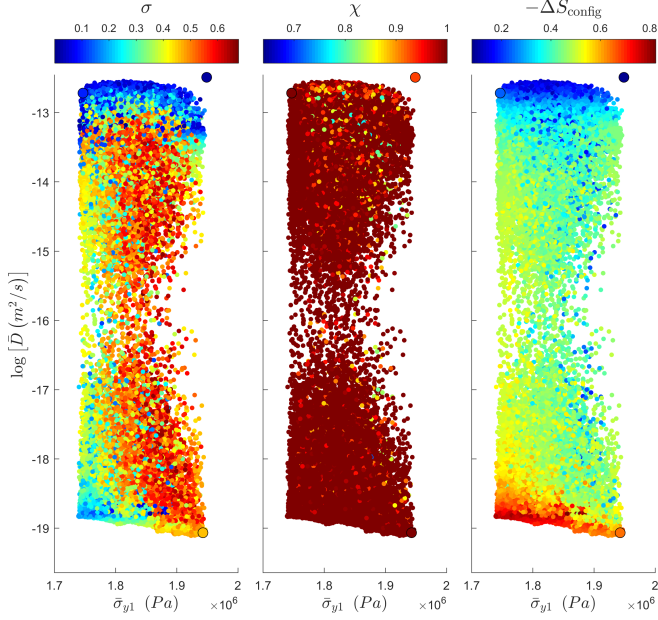
Fig. 12: Plots of the order parameters, σ (left) and χ (center), and negative configurational entropy difference, $-\Delta S_{\text{config}}$ (right) for all of the microstructures in the feasible region. Each marker represents a microstructure, with marker color indicating the corresponding value of the order parameter or $-\Delta S_{\text{config}}$ as shown in the respective colorbars.

which can be determined by the method of Lagrange multipliers [47]. Thus, we follow the convention of [47], and define the negative configurational entropy difference for a grain boundary network as $-\Delta S_{\text{config}} \equiv -\left(S_{\text{config}} - S_{\text{config}}^0\right)$. The larger the value of $-\Delta S_{\text{config}}$ for a microstructure, the less entropic is its configuration (i.e. the more information it contains compared to the maximum entropy configuration). Figure 12 shows that there is a clear trend of decreasing entropy towards the bottom of the feasible region, with the best performing microstructure having $-\Delta S_{\text{config}} = 0.64$ compared to the worst performing microstructure which exhibited $-\Delta S_{\text{config}} = 0.24$. At the same time, there appear to be microstructures whose performance is nearly as good as that of the optimal microstructure, but with significantly higher entropy (note the sharp transition from orange to green above the optimal microstructure), suggesting that with minor sacrifices in performance it may be possible to identify a less extreme microstructural configuration that may be more likely to be observed experimentally or may be more easily manufactured.

8. Conclusions

We have presented a texture-mediated approach to grain boundary network design that facilitates the optimization of microstructures for complex multi-objective design problems. To illustrate its utility we considered a concrete design problem involving the optimization of an Al microstructure intended to be used in a flexible electronics application. In this context we sought to identify a crystallographic texture (as quantified by the ODF) and commensurate grain boundary network structure (as quantified by the TJDF) that would simultaneously maximize the effective yield strength of the polycrystalline material, minimize the grain boundary network diffusivity, and exhibit a specified elastic compliance.

We developed a model that predicts the effective diffusivity of a grain boundary network from the coefficients of its TJDF. Using established texture dependent models for yield strength and elastic compliance, together with our newly developed model for grain boundary network diffusivity, and the relationships between texture and grain boundary network structure derived here and in [6], we computed a properties closure, $\mathscr{P}$, for $\overline{\sigma_{y1}}$, $\overline{S_{1111}}$, and $\overline{D}$. This is the first properties closure that has ever been computed for grain boundary network sensitive properties—or any defect sensitive property for that matter—and represents the envelope of all properties combinations of $\overline{\sigma_{y1}}$, $\overline{S_{1111}}$, and $\overline{D}$ that are predicted to be physically realizable under the assumptions of our constitutive models and the absence of spatially correlated grain orientations. The shape of $\mathscr{P}$ indicates that the properties of interest vary in a complex way with one another, similar to what has been observed in other contexts [43]. For the present design problem, this resulted in competing design objectives.

Using these tools we identified an optimal texture and its corresponding grain boundary network and found that it significantly outperformed both the worst case scenario as well as an "undesigned" isotropic microstructure. This improvement confirms the significant potential for materials properties enhancement that is possible through grain boundary network design.

[1] Lehockey, E.M., Limoges, D., Palumbo, G., Sklarchuk, J., Tomantschger, K., Vincze, A.. On improving the corrosion and growth resistance of positive Pb-acid battery grids by grain boundary engineering. Journal of Power Sources 1999;78(1-2):79–83. URL: http://linkinghub.elsevier.com/retrieve/pii/S0378775399000154. doi:10.1016/S0378-7753(99)00015-4.

[2] Lehockey, E.M., Palumbo, G.. On the creep behaviour of grain boundary engineered nickel. Materials Science and Engineering: A 1997;237(2):168–172. URL: http://linkinghub.elsevier.com/retrieve/pii/S0921509397001263. doi:10.1016/S0921-5093(97)00126-3.

[3] Lehockey, E.M., Palumbo, G., Brennenstuhl, A., Lin, P.. Mitigating intergranular attack and growth in lead-acid battery electrodes for extended cycle and operating life. Metallurgical and Materials Transactions A 1998;29(1):387–396. URL: http://www.springerlink.com/index/T7323GK5257K7K23.pdfhttp://www.springerlink.com/index/10.1007/s11661-998-0190-2. doi:10.1007/s11661-998-0190-2.

[4] Lehockey, E.M., Palumbo, G., Lin, P.. Improving the weldability and service performance of nickel-and iron-based superalloys by grain boundary engineering. Metallurgical and Materials Transactions A 1998;29(12):3069–3079. URL: http://www.springerlink.com/index/10.1007/s11661-998-0214-y. doi:10.1007/s11661-998-0214-y.

[5] Lin, P., Palumbo, G., Erb, U., Aust, K.. Influence of grain boundary character distribution on sensitization and intergranular corrosion of alloy 600. Scripta Metallurgica et Materialia 1995;33(9):1387–1392. URL: http://linkinghub.elsevier.com/retrieve/pii/0956716X9500420Z. doi:10.1016/0956-716X(95)00420-Z.

[6] Johnson, O.K., Schuh, C.A.. The triple junction hull: Tools for grain boundary network design. Journal of the Mechanics and Physics of Solids 2014;69:2–13. URL: http://www.sciencedirect.com/science/article/pii/S0022509614000659. doi:10.1016/j.jmps.2014.04.005.

[7] Johnson, O.K., Schuh, C.A.. The uncorrelated triple junction distribution function: Towards grain boundary network design. Acta Materialia 2013;61(8):2863–2873. URL: http://linkinghub.elsevier.com/retrieve/pii/S1359645413000529. doi:10.1016/j.actamat.2013.01.025.

[8] Adams, B.L., Kalidindi, S.R., Fullwood, D.T.. Microstructure-Sensitive Design for Performance Optimization. 1 ed.; Butterworth-Heinemann; 2012. ISBN 9780123969897. URL: http://books.google.com/books?id=e8miuAAACAAJ. doi:10.1016/B978-0-12-396989-7.01001-7.

[9] Adams, B.L., Henrie, A.J., Henrie, B., Lyon, M., Kalidindi, S.R., Garmestani, H.. Microstructure-sensitive design of a compliant beam. Journal of the Mechanics and Physics of Solids 2001;49(8):1639–1663. URL: http://linkinghub.elsevier.com/retrieve/pii/S0022509601000163. doi:10.1016/S0022-5096(01)00016-3.

[10] Webster, S., Bannister, A.. Structural integrity assessment procedure for Europe - of the SINTAP programme overview. Engineering Fracture Mechanics 2000;67(6):481–514. doi:10.1016/S0013-7944(00)00070-9.

[11] Black, J.. Electromigration-A brief survey and some recent results. IEEE Transactions on Electron Devices 1969;16(4):338–347. URL: http://ieeexplore.ieee.org/search/srchabstract.jsp?tp={\&}arnumber=1475796{\&}queryText=((Document+Title:ElectromigrationA+brief+survey+and+some+recent+results)){\&}openedRefinements=*{\&}sortType=desc{_}Publication+Year{\&}matchBoolean=true{\&}rowsPerPage=50{\&}searchField=Se. doi:10.1109/T-ED.1969.16754.

[12] Hamilton, W.R.. On a new species of imaginary quantities connected with a theory of quaternions. Proceedings of the Royal Irish Academy 1844;2:424–434. URL: http://www.emis.ams.org/classics/Hamilton/Quatern1.pdf.

[13] Mason, J.K., Schuh, C.A.. Hyperspherical harmonics for the representation of crystallographic texture. Acta Materialia 2008;56(20):6141–6155. URL: http://linkinghub.elsevier.com/retrieve/pii/S1359645408005880. doi:10.1016/j.actamat.2008.08.031.

[14] Altmann, S.L.. Rotations, quaternions, and double groups. Mineola: Dover Publications; 2005. ISBN 0486445186.

[15] Mason, J.K.. The relationship of the hyperspherical harmonics to SO(3), SO(4) and orientation distribution functions. Acta crystallographica Section A, Foundations of crystallography 2009;65(Pt 4):259–66. URL: http://www.ncbi.nlm.nih.gov/pubmed/19535847. doi:10.1107/S0108767309009921.

[16] Bollmann, W.. Triple lines in polycrystalline aggregates as disclinations. Philosophical Magazine A 1984;49(1):73–79. URL: http://www.tandfonline.com/doi/abs/10.1080/01418618408233430. doi:10.1080/01418618408233430.

[17] Frary, M.E., Schuh, C.A.. Combination rule for deviant CSL grain boundaries at triple junctions. Acta Materialia 2003;51(13):3731–3743. URL: http://linkinghub.elsevier.com/retrieve/pii/S1359645403001885. doi:10.1016/S1359-6454(03)00188-5.

[18] Sachs, G.. Zur Ableitung einer Fließbedingung. Zeitschrift des Vereines Deutscher Ingenieure 1928;72(22):734.

[19] Wu, X., Proust, G., Knezevic, M., Kalidindi, S.R.. Elasticplastic property closures for hexagonal close-packed polycrystalline metals using first-order bounding theories. Acta Materialia 2007;55(8):2729–2737. URL: http://linkinghub.elsevier.com/retrieve/pii/S1359645407000171. doi:10.1016/j.actamat.2006.12.010.

[20] Tiryakioglu, M., Staley, J.T.. Physical Metallurgy and the Effect of Alloying Additions in Aluminum Alloys. In: Totten, G.E., Mackenzie, D.S., editors. Handbook of Aluminum Vol. 1: Physical Metallurgy

and Processes; chap. 3. New York: CRC Press. ISBN 978-0-8247-0494-0; 2003, p. 81–210. URL: http://dx.doi.org/10.1201/9780203912591.ch3. doi:10.1201/9780203912591.ch3.

[21] Fullwood, D.T., Niezgoda, S.R., Adams, B.L., Kalidindi, S.R.. Microstructure sensitive design for performance optimization. Progress in Materials Science 2010;55(6):477–562. URL: http://linkinghub.elsevier.com/retrieve/pii/S0079642509000760. doi:10.1016/j.pmatsci.2009.08.002.

[22] Voigt, W.. Lehrbuch der Kristallphysik. Leipzig: B.G. Teubner Verlag; 1928.

[23] Bunge, H.J.. Texture Analysis in Materials Science: Mathematical Methods. 3 ed.; Cuvillier; 1993. ISBN 3928815814.

[24] Frederikse, H.P.R.. Elastic Constants of Single Crystals General References. In: Haynes, W.M., editor. CRC Handbook of Chemistry and Physics; chap. 12; 94 ed. Boca Raton, FL: CRC Press/Taylor & Francis. ISBN 978-1466571143; 2013, p. (12)35–(12)40.

[25] Chen, Y., Schuh, C.a.. Diffusion on grain boundary networks: Percolation theory and effective medium approximations. Acta Materialia 2006;54(18):4709–4720. URL: http://linkinghub.elsevier.com/retrieve/pii/S1359645406004265. doi:10.1016/j.actamat.2006.06.011.

[26] Frary, M.E., Schuh, C.A.. Correlation-space description of the percolation transition in composite microstructures. Physical Review E 2007;76(4):42–45. URL: http://link.aps.org/doi/10.1103/PhysRevE.76.041108. doi:10.1103/PhysRevE.76.041108.

[27] Reed, B.W., Schuh, C.A.. Grain Boundary Networks. In: Schwartz, A.J., Kumar, M., Adams, B.L., Field, D.P., editors. Electron Backscatter Diffraction in Materials Science; chap. 15; 2 ed. New York, New York, USA: Springer US. ISBN 978-0-387-88135-5; 2009, p. 201–214. URL: http://www.springerlink.com/index/10.1007/978-0-387-88136-2. doi:10.1007/978-0-387-88136-2.

[28] McLachlan, D.S.. The correct modelling of the second order terms of the complex AC conductivity results for continuum percolation media, using a single phenomenological equation. Physica B: Condensed Matter 2003;338(1-4):256–260. URL: http://linkinghub.elsevier.com/retrieve/pii/S0921452603005076. doi:10.1016/j.physb.2003.08.002.

[29] McLachlan, D.S.. An equation for the conductivity of binary mixtures with anisotropic grain structures. Journal of Physics C: Solid State Physics 1987;20(7):865–877. URL: http://stacks.iop.org/0022-3719/20/i=7/a=004?key=crossref.dc03dc71811bffbd32c41f06ed2ec03b. doi:10.1088/0022-3719/20/7/004.

[30] Schuh, C.A., Minich, R.W., Kumar, M.. Connectivity and percolation in simulated grain-boundary networks. Philosophical Magazine 2003;83(6):711–726. URL: http://www.tandfonline.com/doi/abs/10.1080/0141861021000056681. doi:10.1080/0141861021000056681.

[31] Frary, M.E., Schuh, C.A.. Percolation and statistical properties of low- and high-angle interface networks in polycrystalline ensembles. Physical Review B 2004;69(13):134115. URL: http://link.aps.org/doi/10.1103/PhysRevB.69.134115. doi:10.1103/PhysRevB.69.134115.

[32] Frary, M.E., Schuh, C.A.. Grain boundary networks: Scaling laws, preferred cluster structure, and their implications for grain boundary engineering. Acta Materialia 2005;53(16):4323–4335. URL: http://linkinghub.elsevier.com/retrieve/pii/S1359645405003319. doi:10.1016/j.actamat.2005.05.030.

[33] Kaur, I., Gust, W.. Handbook of Grain and Interphase Boundary Diffusion Data; vol. 1. 1 ed.; Stuttgart: Ziegler Press; 1989.

[34] Grimmer, H.. A unique description of the relative orientation of neighbouring grains. Acta Crystallographica Section A 1980;36(3):382–389. URL: http://scripts.iucr.org/cgi-bin/paper?S0567739480000861. doi:10.1107/S0567739480000861.

[35] Johnson, O.K., Li, L., Demkowicz, M.J., Schuh, C.A.. Inferring grain boundary structureproperty relations from effective property measurements. Journal of Materials Science 2015;50(21):6907–6919. URL: http://link.springer.com/10.1007/s10853-015-9241-4. doi:10.1007/s10853-015-9241-4.

[36] Biscondi, M.. Intergranular diffusion and grain-boundary structure. In: Lacombe, P., editor. Physical Chemistry of the Solid State: Applications to Metals and their Compounds. Amsterdam: Elsevier Science Publishers B.V.; 1984, p. 225–239.

[37] Barber, C.B., Dobkin, D.P., Huhdanpaa, H.. The quickhull algorithm for convex hulls. ACM Transactions on Mathematical Software 1996;22(4):469–483. doi:10.1145/235815.235821.

[38] Johnson, O.K., Kurniawan, C.. An Efficient Algorithm for Generating Diverse Microstructure Sets and Delineating Properties Closures. (Submitted) 2017;.

[39] Johnson, O.K., Schuh, C.A.. Texture mediated grain boundary network design in two dimensions. Journal of Materials Research 2016;31(09):1171–1184. URL: http://journals.cambridge.org/abstract{_}S0884291416001382http://www.journals.cambridge.org/abstract{_}S0884291416001382. doi:10.1557/jmr.2016.138.

[40] Ebert, T., Belz, J., Nelles, O.. Interpolation and extrapolation: Comparison of definitions and survey of algorithms for convex and concave hulls. In: 2014 IEEE Symposium on Computational Intelligence and Data Mining (CIDM). ISBN 978-1-4799-4518-4; 2014, p. 310–314. URL: http://ieeexplore.ieee.org/lpdocs/epic03/wrapper.htm?arnumber=7008683. doi:10.1109/CIDM.2014.7008683.

[41] Edelsbrunner, H., Mücke, E.. Three-dimensional alpha shapes. ACM Transactions on Graphics 1994;13(1):32. URL: http://arxiv.org/abs/math/9410208. doi:10.1145/174462.156635. arXiv:9410208.

[42] Edelsbrunner, H., Kirkpatrick, D.,

Seidel, R.. On the shape of a set of points in the plane. IEEE Transactions on Information Theory 1983;29(4):551--559. doi:10.1109/TIT.1983.1056714.

[43] Lyon, M., Adams, B.L.. Gradient-based non-linear microstructure design. Journal of the Mechanics and Physics of Solids 2004;52(11):2569--2586. URL: http://linkinghub.elsevier.com/retrieve/pii/S0022509604000857. doi:10.1016/j.jmps.2004.04.009.

[44] Adams, B.L., Kalidindi, S.R., Fullwood, D.T.. Second-Order Hull, Property Closure, and Design 14. In: Microstructure-Sensitive Design for Performance Optimization; 1 ed. Waltham: Butterworth-Heinemann. ISBN 9780123969897; 2012, p. 303--330. doi:10.1016/B978-0-12-396989-7.00014-9.

[45] Patala, S., Mason, J.K., Schuh, C.A.. Improved representations of misorientation information for grain boundary science and engineering. Progress in Materials Science 2012;57(8):1383--1425. URL: http://linkinghub.elsevier.com/retrieve/pii/S0079642512000370. doi:10.1016/j.pmatsci.2012.04.002.

[46] Patala, S., Schuh, C.A.. A continuous and one-to-one coloring scheme for misorientations. Acta Materialia 2011;59(2):554--562. URL: http://linkinghub.elsevier.com/retrieve/pii/S135964541000635X. doi:10.1016/j.actamat.2010.09.058.

[47] Frary, M.E., Schuh, C.A.. Connectivity and percolation behaviour of grain boundary networks in three dimensions. Philosophical Magazine 2005;85(11):1123--1143. URL: http://www.informaworld.com/openurl?genre=article{\&}doi=10.1080/14786430412331323564{\&}magic=crossref||D404A21C5BB053405B1A640AFFD44AE3http://www.tandfonline.com/doi/abs/10.1080/14786430412331323564. doi:10.1080/14786430412331323564.